NANOMEDICINE

Imaging-assisted nanoimmunotherapy for atherosclerosis in multiple species

Tina Binderup[1,2]*, Raphaël Duivenvoorden[1,3]*, Francois Fay[1,4]*, Mandy M. T. van Leent[1], Joost Malkus[1], Samantha Baxter[1], Seigo Ishino[1], Yiming Zhao[1], Brenda Sanchez-Gaytan[1], Abraham J. P. Teunissen[1], Yohana C. A. Frederico[1], Jun Tang[1,5], Giuseppe Carlucci[5,6], Serge Lyaschenko[5,7], Claudia Calcagno[1], Nicolas Karakatsanis[1], Georgios Soultanidis[1], Max L. Senders[1,8], Philip M. Robson[1], Venkatesh Mani[1], Sarayu Ramachandran[1], Mark E. Lobatto[1,9], Barbara A. Hutten[10], Juan F. Granada[11], Thomas Reiner[5,7], Filip K. Swirski[12], Matthias Nahrendorf[12], Andreas Kjaer[2], Edward A. Fisher[13], Zahi A. Fayad[1]†, Carlos Pérez-Medina[1,14], Willem J. M. Mulder[1,8,15,16]†

Nanomedicine research produces hundreds of studies every year, yet very few formulations have been approved for clinical use. This is due in part to a reliance on murine studies, which have limited value in accurately predicting translational efficacy in larger animal models and humans. Here, we report the scale-up of a nanoimmunotherapy from mouse to large rabbit and porcine atherosclerosis models, with an emphasis on the solutions we implemented to overcome production and evaluation challenges. Specifically, we integrated translational imaging readouts within our workflow to both analyze the nanoimmunotherapeutic's in vivo behavior and assess treatment response in larger animals. We observed our nanoimmunotherapeutic's anti-inflammatory efficacy in mice, as well as rabbits and pigs. Nanoimmunotherapy-mediated reduction of inflammation in the large animal models halted plaque progression, supporting the approach's translatability and potential to acutely treat atherosclerosis.

INTRODUCTION

The nanomedicine research field continues to grow, with hundreds of new nanoformulations reported every year. However, comparatively few formulations are clinically translated to benefit patients. The overwhelming majority of preclinical work is limited to proof-of-concept mouse studies, and serious concerns have been raised about these studies' relevance, particularly in relation to efficient nanomedicine drug delivery in patients (1). At the same time, a paradigm shift in the nanomedicine field has gained momentum as new nanotherapies are being designed to deliberately engage the immune system (2, 3) rather than evading it, which has been nanomedicine's primary focus for decades. The ability to selectively modulate the immune response via nanomedicines (4, 5), nanoimmunotherapy, is reinvigorating the field. This approach can treat conditions, such as cancer, atherosclerosis, or autoimmune diseases, in which a dysregulated immune response is either an underlying or a contributing factor. In the past decade, we have pioneered nanoimmunotherapeutic approaches to treat atherosclerosis, a chronic inflammatory disorder of medium and large arteries that is the major underlying cause of cardiovascular disease. We developed a myeloid cell–specific nanoimmunotherapy that rapidly and efficiently silences vessel wall inflammation (6) by inhibiting macrophage proliferation (7).

Such nanoimmunotherapies can be translationally relevant if two key challenges are addressed. First, orders of magnitude more nanomaterial must be produced for larger animals and humans than for mice. Producing multigram amounts in a controlled and reproducible manner requires developing alternatives to traditional benchtop formulation methods. Second, the markedly lower number of large animals that can be reasonably included in a translational study necessitates different therapeutic readouts than those typically used in mouse studies. Concurrently, successful translation crucially requires developing both techniques to quantitatively determine the nanoimmunotherapeutic's distribution in the body after administration and related noninvasive imaging methods to probe this over time (8).

Here, we report a strategy that surmounts the aforementioned translation hurdles to help to close the daunting gap between benchtop and bedside nanomedicine research. Our approach involves scaling up a nanoimmunotherapeutic production strategy using a microfluidizer-based high-pressure homogenization process and its imaging-guided evaluation in three different atherosclerosis animal models. After establishing the high-pressure homogenization-produced nanoimmunotherapy's efficacy in atherosclerotic mice, we performed noninvasive assessments of its in vivo behavior and treatment response in atherosclerotic rabbits and pigs by integrated positron emission tomography (PET) magnetic resonance imaging (MRI).

[1]Translational and Molecular Imaging Institute, Icahn School of Medicine at Mount Sinai, New York, NY 10029, USA. [2]Department of Clinical Physiology, Nuclear Medicine and PET and Cluster for Molecular Imaging, Department of Biomedical Sciences, Rigshospitalet and University of Copenhagen, 2100 Copenhagen, Denmark. [3]Department of Nephrology, Radboud Institute for Molecular Life Sciences, Radboud University Medical Center, 6525 XZ Nijmegen, Netherlands. [4]Institut Galien Paris Sud, Faculté de Pharmacie, CNRS, Univ. Paris-Sud, Université Paris-Saclay, 92290 Châtenay-Malabry, France. [5]Department of Radiology, Memorial Sloan Kettering Cancer Center, New York, NY 10065, USA. [6]Bernard and Irene Schwarz Center for Biomedical Imaging, New York University, New York, NY 10016, USA. [7]Department of Radiology, Weill Cornell Medical College, New York, NY 10065, USA. [8]Department of Medical Biochemistry, Amsterdam University Medical Centers, University of Amsterdam, 1105 AZ Amsterdam, Netherlands. [9]Department of Radiology, Spaarne Gasthuis, 2035 RC Haarlem, Netherlands. [10]Department of Clinical Epidemiology, Biostatistics and Bioinformatics, Amsterdam University Medical Centers, 1105 AZ Amsterdam, Netherlands. [11]CRF Skirball Center for Innovation, Cardiovascular Research Foundation, Orangeburg, NY 10962, USA. [12]Center for Systems Biology and Department of Radiology, Massachusetts General Hospital, Harvard Medical School, Boston, MA 02114, USA. [13]Department of Medicine (Cardiology) and Cell Biology, Marc and Ruti Bell Program in Vascular Biology, New York University School of Medicine, New York, NY 10016, USA. [14]Centro Nacional de Investigaciones Cardiovasculares Carlos III, 28029 Madrid, Spain. [15]Department of Oncological Sciences, Icahn School of Medicine at Mount Sinai, New York, NY 10029, USA. [16]Laboratory of Chemical Biology, Department of Biomedical Engineering and Institute for Complex Molecular Systems, Eindhoven University of Technology, 5612 AZ Eindhoven, Netherlands.
*These authors contributed equally to this work.
†Corresponding author. Email: willem.mulder@mssm.edu (W.J.M.M.); zahi.fayad@mssm.edu (Z.A.F.)

We thus demonstrate the translatability of our nanoimmunotherapeutic approach and its ability to acutely treat vessel wall inflammation in atherosclerosis.

RESULTS

Development and production scale-up of S-HDL nanoimmunotherapy

In three recent publications, we reported the development of a simvastatin-loaded high-density lipoprotein (S-HDL) nanotherapeutic that we successfully applied in atherosclerosis mouse models to treat vessel wall inflammation (6, 7, 9). However, because of its low production rate (120 mg/hour), our original benchtop sonication-based S-HDL production method was not suitable to generate the necessary amounts for studies in large animal models. Therefore, we designed and implemented a high-pressure homogenization process, including innovative purification methods, to scale up S-HDL production and generate the required amounts (Fig. 1A).

We first implemented a large-scale apolipoprotein A1 (APOA1) extraction method. Using the optimized workflow described in Materials and Methods, we isolated 10 g of APOA1 from purified human HDL, which is one order of magnitude more than we could previously generate. Our previously reported benchtop S-HDL formulation method involves hydrating a film composed of phospholipids and simvastatin with a buffered APOA1 solution, followed by 1 hour of sonication and multiple purification steps (6, 7). The new production method also uses the formation of a dry film, albeit one containing at least 40 times more phospholipid/simvastatin. After the film's complete hydration with 0.5 liters of an APOA1-containing saline buffer in the appropriate ratio, the suspension was homogenized using the microfluidizer 110-S Processor (Microfluidics). This high-pressure homogenization method processes batches containing 5 g of total bulk ingredients in 30 min, leading to an 80-fold higher production rate compared to our original method. Because of the large amount of S-HDL produced, we scaled the purification steps using tangential flow filtration and funnel vacuum filtration methods. This process enabled the production of up to 18 g (total bulk ingredients) of S-HDL per production run, with a simvastatin recovery of 67 ± 6% (n = 8; table S1), yielding discoidal S-HDL particles (Fig. 1A and fig. S1A) with a mean diameter of 23.6 ± 3.7 nm (dispersity index: 0.24 ± 0.04, n = 8). These morphological features are comparable to S-HDL prepared using our original benchtop method (6, 7). We produced a total of about 90 g of S-HDL nanoimmunotherapeutic with suitable physicochemical properties for in vivo application. An overview of all individual batches' physicochemical properties is provided in table S1.

An in vitro comparison study between benchtop- and microfluidizer-produced S-HDL was conducted on murine bone marrow–derived macrophages (BMDMs). Cell viability and proliferation experiments on BMDMs revealed the therapeutic effects of both formulations to be very similar (fig. S1, B to D). In addition, both formulations were labeled with the fluorescent dye DiO, yielding DiO-S-HDL, to enable their visualization by optical techniques. Confocal laser scanning microscopy revealed both DiO-S-HDL formulations to associate with BMDMs in a similar fashion (fig. S1E).

To enable quantitative assessment of our nanoimmunotherapeutic's blood half-life and biodistribution, we developed a ^{89}Zr-labeled S-HDL analog ([^{89}Zr]-S-HDL; Fig. 1B) following a strategy that we previously reported (10). Briefly, we included the phospholipid chelator

3-((hydroxy(2-(3-(4-(3-(3,14,25-trihydroxy-2,10,13,21,24-pentaoxo-3,9,14,20,25-pentaazatri-acontan-30-yl)thioureido)phenyl)thioureido) ethoxy) phosphoryl)oxy)propane-1,2-diyldistearate (DSPE-DFO) in the formulation to allow radiolabeling with ^{89}Zr. Radiolabeling was performed by reacting with [^{89}Zr]zirconium (IV) oxalate, and radiochemically pure [^{89}Zr]-S-HDL (fig. S1F) was obtained in high yield (>85%). The radiolabeling allowed localization of our nanobiologic by in vivo PET imaging.

S-HDL biodistribution, cellular specificity, and therapeutic efficacy in Apoe$^{-/-}$ mice

In three previously reported studies, we extensively evaluated benchtop-produced S-HDL's therapeutic efficacy in atherosclerotic apolipoprotein E–deficient (Apoe$^{-/-}$) mice (6, 7, 9). To ensure that the S-HDL produced in large batches by high-pressure homogenization exerts similar therapeutic effects, we first conducted mouse experiments. We studied [^{89}Zr]-S-HDL's in vivo behavior in Apoe$^{-/-}$ mice that had been fed a Western diet for 12 weeks to induce advanced atherosclerosis. The blood radioactivity half-life was 3.1 hours (two-phase decay, weighted $t_{1/2}$; Fig. 1C), which is comparable to the blood half-life of other HDL nanobiologics (2). PET imaging at 24 hours after injection showed [^{89}Zr]-S-HDL's accumulation in the spleen, kidneys, liver, and periaortic lymph nodes (Fig. 1D). PET imaging data were complemented by ex vivo gamma counting results (Fig. 1E). Digital autoradiography of excised aortas revealed high radioactivity deposition in the aortic arch and roots, indicating high accumulation of our nanoimmunotherapy in atherosclerotic lesions (Fig. 1E).

In vivo cellular specificity of microfluidizer-produced DiO-S-HDL was studied in atherosclerotic Apoe$^{-/-}$ mice. Twenty-four hours after intravenous administration of DiO-S-HDL, mice were sacrificed, and their spleens and aortas harvested and processed. Flow cytometry revealed preferential myeloid cell targeting in the aorta (Fig. 1, F and G), similar to benchtop-produced S-HDL (fig. S2A). The cellular affinity profile in the spleen was nearly identical for both benchtop- and microfluidizer-produced formulations (fig. S2, B and C).

Subsequently, we investigated the anti-atherosclerotic efficacy of the S-HDL formulation produced by high-pressure homogenization in Apoe$^{-/-}$ mice with advanced atherosclerosis. As readouts, we combined whole aorta flow cytometry (Fig. 1H) and histological analysis of cross sections of the aortic arch, which is where plaque development is most reproducible in this mouse model. We found that delivering four infusions of S-HDL (simvastatin dose, 60 mg/kg per infusion) within 1 week decreased aortic macrophage numbers by 45% (P < 0.05; Fig. 1I). Representative images from aortic arch histological sections are shown in Fig. 1J. Collectively, these results demonstrate that microfluidizer-produced S-HDL's biodistribution, cellular specificity, and therapeutic efficacy mirror those of benchtop-produced S-HDL (7). This marks an important advancement because production scale-up is a prerequisite for translation to large animal models and, ultimately, the ability to conduct human studies.

S-HDL nanoimmunotherapy translation to large animal models of atherosclerosis

The results of our mouse model experiments incentivized us to proceed with testing S-HDL in large animal models of atherosclerosis, namely, rabbit and porcine models. Both are well-established atherosclerosis models in which plaque development is induced by a combination of Western diet and surgical denudation of the endothelium, resulting in accelerated plaque development (Fig. 2A). In the rabbit model,

Binderup et al., Sci. Transl. Med. 11, eaaw7736 (2019)   21 August 2019

2 of 13
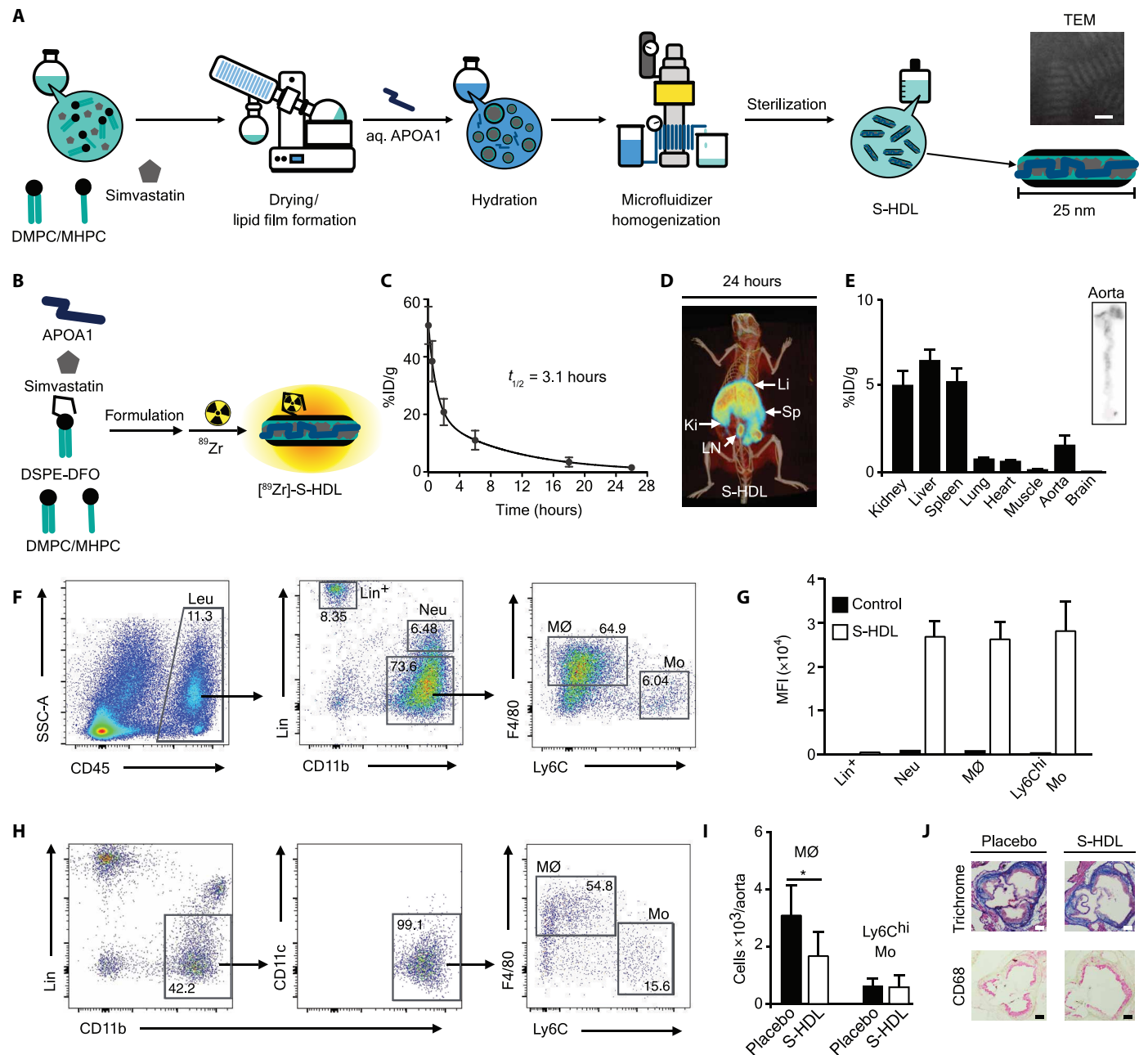
Fig. 1. Nanoimmunotherapy production scale-up and evaluation in *Apoe*^{−/−} mice. (**A**) Schematic of S-HDL production by high-pressure microfluidic homogenization. Transmission electron microscopy (TEM) image of S-HDL. Scale bar, 25 nm. (**B**) Schematic of radiolabeling of S-HDL with ^{89}Zr by incorporating the phospholipid chelator DSPE-DFO in the formulation. (**C**) Blood time-activity curve for [^{89}Zr]-S-HDL intravenously injected in *Apoe*^{−/−} mice ($n = 4$; 12 weeks on Western diet). ID, injected dose. (**D**) Representative 3D-rendered PET/CT fusion image of an *Apoe*^{−/−} mouse 26 hours after injection of [^{89}Zr]-S-HDL. (**E**) Quantitation of tissue radioactivity distribution 26 hours after injection of [^{89}Zr]-S-HDL in *Apoe*^{−/−} mice ($n = 4$; 12 weeks on Western diet). On the right, representative autoradiograph showing radioactivity distribution on the aorta of an *Apoe*^{−/−} mouse 26 hours after injection of [^{89}Zr]-S-HDL. (**F**) Gating procedure used in the flow cytometry evaluation of microfluidizer-produced DiO-S-HDL's cell specificity in *Apoe*^{−/−} mouse aortas. (**G**) DiO mean fluorescence intensity (MFI) in different cell types from *Apoe*^{−/−} mouse aortas. Control, uninjected animal. (**H**) Gating procedure used in the flow cytometry analysis to evaluate S-HDL treatment efficacy in aortas of *Apoe*^{−/−} mice. (**I**) Quantitation of aortic macrophages (MØ) and monocytes (Ly6C^{hi} Mo) after treatment with PBS (placebo) or S-HDL in *Apoe*^{−/−} mice ($n = 10$ per group; 12 weeks on Western diet). (**J**) Representative aortic sections from *Apoe*^{−/−} mice ($n = 2$ per group; 12 weeks on Western diet) treated with PBS (placebo) or S-HDL. Scale bars, 200 μm. CD68 is expressed on macrophages. aq., aqueous; Li, liver; Sp, spleen; Ki, kidney; LN, lymph node; Leu, leukocyte; Lin⁺, lineage positive; Neu, neutrophil. Data are presented as means ± SD from one experiment. *$P < 0.05$ (Mann-Whitney test).

aortic angioplasty was performed, whereas in the swine model, lesions were induced in the femoral arteries. The therapeutic dose was calculated from human equivalent dose tabulated values from the U.S.

Food and Drug Administration (*11*) based on body weight and surface area. Drawing on our previous studies in mice, we used 60 mg of simvastatin per kilogram of body weight (180 mg/m² surface area)
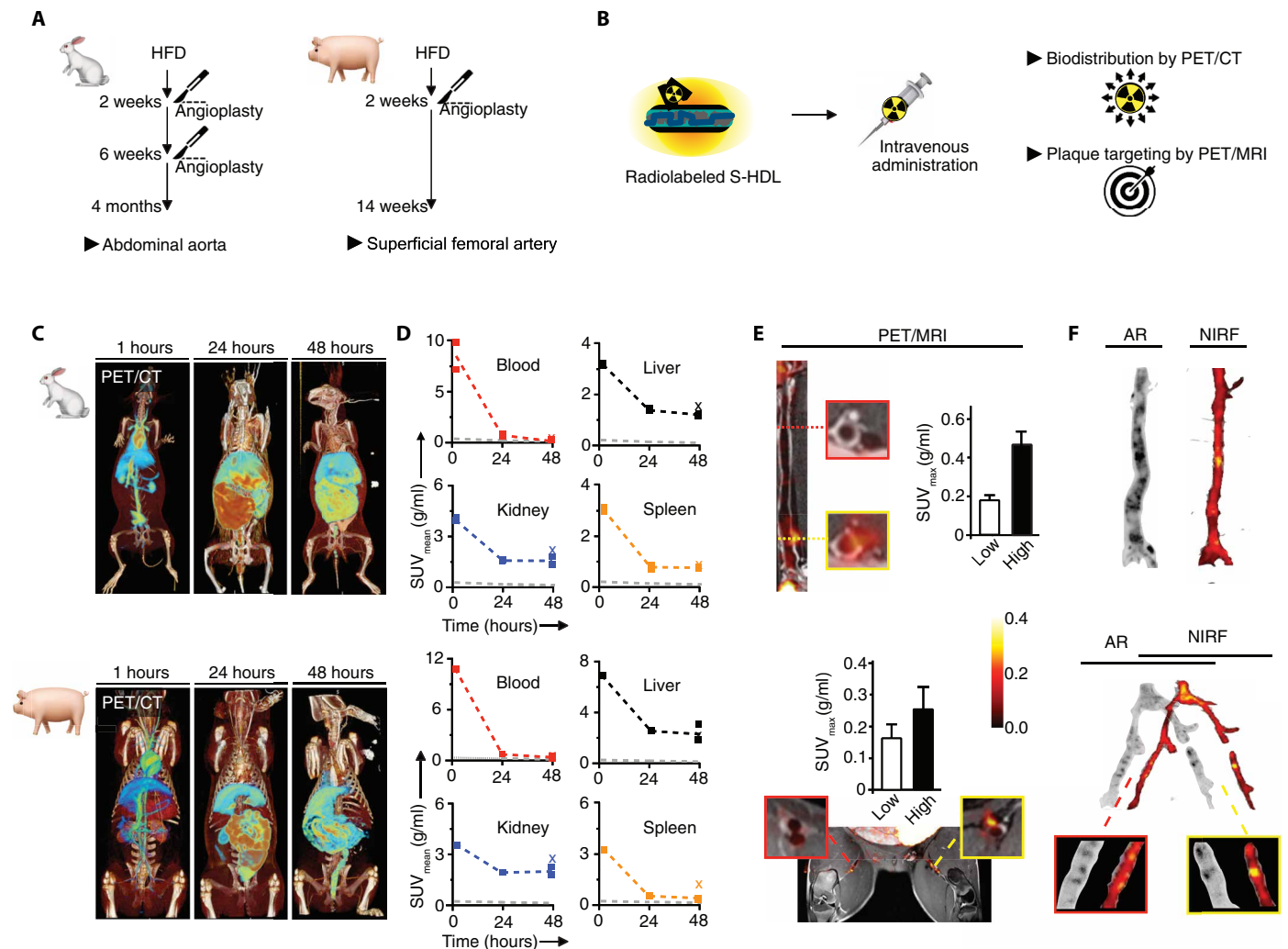
Fig. 2. S-HDL nanoimmunotherapy in vivo evaluation by noninvasive imaging in rabbits and pigs. (**A**) Schematic description of the rabbit and porcine atherosclerosis models used in this study. (**B**) Schematic of noninvasive biodistribution and plaque targeting using ^{89}Zr-S-HDL with PET/CT and PET/MRI, respectively. (**C**) Representative 3D-rendered PET/CT fusion images of atherosclerotic rabbits (top) and pigs (bottom) at 1, 24, and 48 hours after administration of [^{89}Zr]-S-HDL. (**D**) PET imaging–derived time-activity curves in selected tissues in rabbits ($n = 2$; top) and pigs ($n = 2$; bottom) injected with [^{89}Zr]-S-HDL. The x represents the value obtained ex vivo by gamma counting. The gray line is the muscle time-activity curve, included for reference. (**E**) PET/MRI assessment of plaque targeting and quantification of standardized uptake values (SUVs) in one rabbit (top) and one pig (bottom), 48 hours after injection of [^{89}Zr]-S-HDL, in the low and high uptake regions shown in the red- and yellow-bordered squares, respectively. Data shown in (D) and (E) were obtained from one experiment; no statistical analysis was carried out because of the limited number of subjects ($n \leq 2$). (**F**) Regional distribution of S-HDL in atherosclerotic samples from rabbits (top) and pigs (bottom), as determined by autoradiography (AR; [^{89}Zr]-S-HDL) and near-infrared fluorescence (NIRF; DiD-S-HDL) 48 hours after injection.

as a starting point and applied a ratio between correction factors (K_m) of the different species. The calculated rabbit and pig doses were 15 mg/kg (K_m ratio = 1:4) and 7.5 mg/kg (K_m ratio = 1:8), respectively.

Our translational evaluation encompassed PET imaging of biodistribution and plaque targeting (Fig. 2, B to F) and a noninvasive imaging-based assessment of treatment response (Figs. 3 and 4). These protocols were developed and evaluated in a separate cohort of six pigs not included in the ensuing biodistribution and therapeutic experiments. Protocol development included optimizing imaging parameters for (i) noncontrast-enhanced time-of-flight (TOF) magnetic resonance (MR) angiography to identify the aorta and femoral arteries; (ii) three-dimensional (3D), isotropic, high-resolution black blood vessel wall MRI for plaque quantification in the whole femoral

arterial tree; and (iii) 3D black blood dynamic contrast–enhanced (DCE)–MRI with high spatial resolution and coverage to quantify plaque endothelial permeability. Specifically, flip angle and number of imaging slabs were varied for TOF angiography until adequate coverage and blood pool contrast were obtained. For 3D black blood vessel wall and DCE-MRI, the acquisition plane, number of acquired slices, spatial resolution, and number of signal averages were optimized to obtain high signal-to-noise ratios and to minimize blood pool signal for adequate vessel wall delineation.

In vivo PET imaging of S-HDL in atherosclerotic rabbits and pigs

First, we performed in vivo PET/computed tomography (CT) imaging to assess biodistribution and pharmacokinetics in atherosclerotic
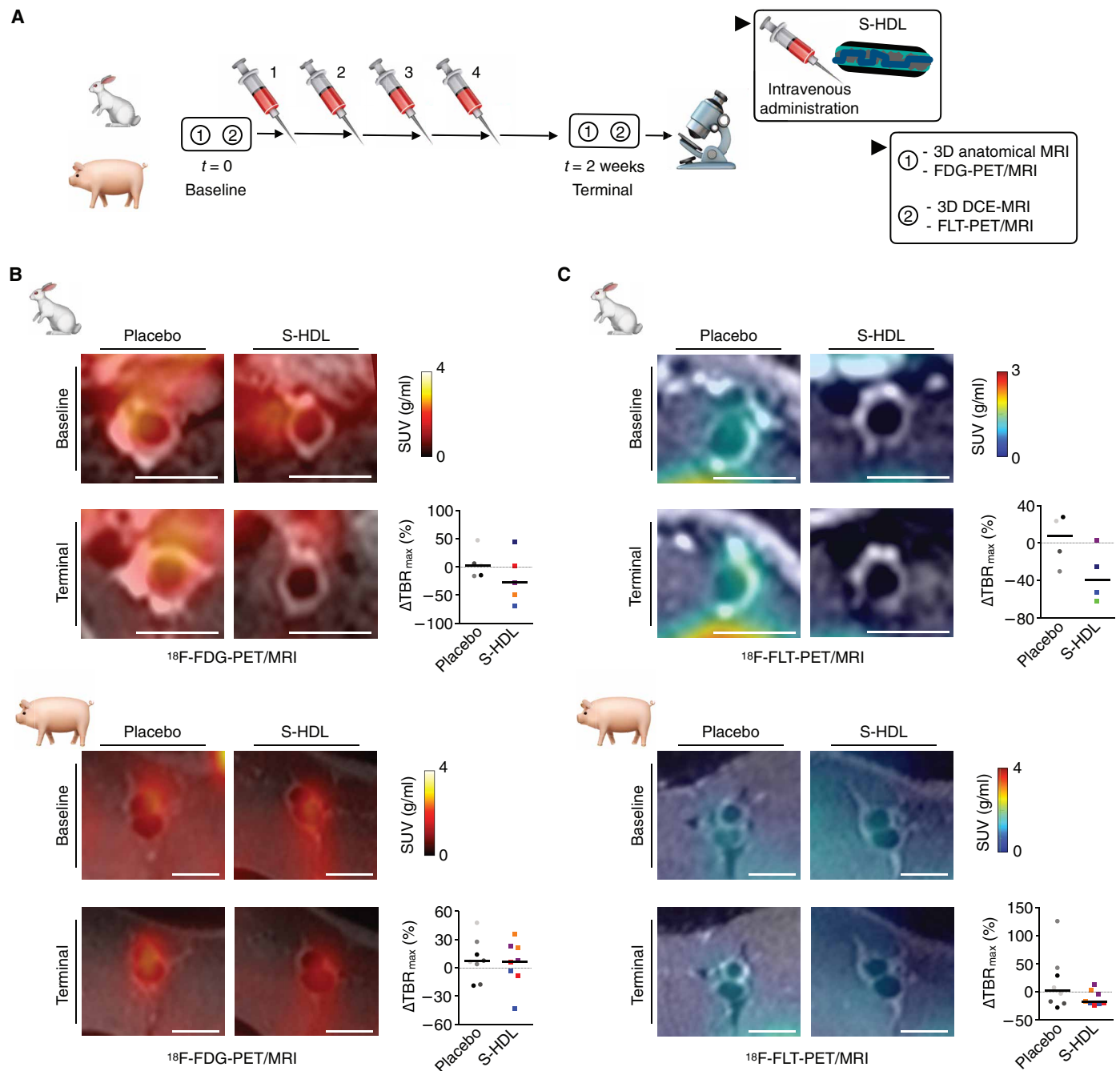
Fig. 3. Imaging-guided S-HDL nanoimmunotherapy in rabbits and pigs: PET-based readouts. (**A**) Schematic representation of S-HDL imaging–guided treatment. Treatment response was evaluated longitudinally by performing a baseline scan before the first S-HDL administration and a terminal scan 48 hours after the last infusion. Animals received four infusions over 2 weeks. (**B**) ^{18}F-FDG-PET imaging–based assessment of vessel wall inflammation in rabbits ($n = 5$ per group; top) and pigs ($n = 4$ per group; bottom) treated with PBS (placebo) or S-HDL. Scale bars, 10 mm. (**C**) ^{18}F-FLT-PET imaging–based assessment of cellular proliferation in the vessel wall in rabbits ($n = 4$ per group; top) and pigs ($n = 4$ per group; bottom) treated with PBS (placebo) or S-HDL. Scale bars, 10 mm. In (B) and (C), dots are color-coded for individual animals, and two data points are represented per pig, corresponding to values obtained from analysis of each of the femoral arteries. Line is situated at median. TBR$_{max}$, maximal target-to-background ratio. Data were obtained in one experiment and analyzed using a linear mixed model (see the "Statistical analysis" section for details).

rabbits and pigs. Rabbits ($n = 2$) and pigs ($n = 2$) were infused with [89Zr]-S-HDL. One rabbit and one pig were coinjected with DiD-S-HDL to validate targeting ex vivo. Whole-body static scans were acquired 1, 24, and 48 hours after injection. Images were initially dominated by a high blood pool signal (1 hour), followed by liver

and intestinal accumulation (24 and 48 hours), consistent with hepatobiliary excretion (Fig. 2C). The clearance kinetics (fig. S3A) and radioactivity distribution pattern were similar in both species, with liver and kidneys as the main accumulation sites (Fig. 2D).

Binderup *et al.*, *Sci. Transl. Med.* **11**, eaaw7736 (2019)   21 August 2019

5 of 13

After the last PET/CT scan (48 hours after injection), PET/MRI was performed in [^{89}Zr]-S-HDL–injected rabbits and pigs to assess plaque targeting in vivo. Obvious focal vessel wall accumulation in rabbits' abdominal aortas and pigs' femoral arteries was visualized (Fig. 2E). In these regions, radioactivity concentration was more than twofold higher than in uninjured arterial fragments (Fig. 2E). We performed near-infrared fluorescence (NIRF) imaging with DiD-S-HDL (one rabbit and one pig) and Evans Blue (one rabbit and one pig) to evaluate plaque targeting and vessel wall permeability, respectively. The corresponding arterial samples were compared against [^{89}Zr]-S-HDL autoradiography. DiD-S-HDL and [^{89}Zr]-S-HDL were colocalized in plaque (Fig. 2F), whereas [^{89}Zr]-S-HDL and Evans Blue (fig. S3B) had a different distribution pattern in both rabbit and pig samples, revealing that HDL nanobiologics' accumulation in the vessel wall is not merely governed by microvessel permeability. The discrepancy between Evans Blue and HDL nanobiologics' accumulation patterns corroborates our previous observations (12) that HDL nanobiologics' plaque accumulation is due to their inherent avidity for macrophages (6, 7, 10, 12).

PET/MRI of S-HDL anti-atherosclerotic activity

Next, we investigated the efficacy of S-HDL therapy in large animal atherosclerosis models. Rabbits and pigs received four intravenous S-HDL infusions using simvastatin doses of 15 and 7.5 mg/kg, respectively. The infusions were given over the course of 2 weeks. We noninvasively and longitudinally evaluated therapeutic response using a multiparametric PET/MRI protocol (Fig. 3A). Four different atherosclerosis-related parameters were measured, namely, (i) vessel wall inflammation by ^{18}F-labeled 2-deoxy-2-fluoro-D-glucose (^{18}F-FDG)–PET, (ii) cellular proliferation by ^{18}F-labeled 3'-fluoro-3'-deoxythymidine (^{18}F-FLT)–PET, (iii) vessel wall permeability by in vivo DCE-MRI (and ex vivo by Evans Blue NIRF imaging), and (iv) vessel wall thickness by T2-weighted MRI. Imaging sessions were performed at baseline and 2 weeks after the onset of therapy. Imaging was performed on the aorta in rabbits and on the femoral arteries in pigs.

We used a linear mixed model (LMM) to statistically analyze differences in imaging-derived parameters between treatment groups. The imaging parameter at the end of the study (terminal scan) was used as the dependent variable. Type of treatment and imaging parameter at the start of the study (baseline) were defined as fixed effects, and the side (left or right femoral artery in pigs) was defined as a random effect. On the basis of this analysis, vessel wall inflammation, as measured by ^{18}F-FDG-PET (Fig. 3B), was not different between the S-HDL and placebo groups [LMM $P = 0.292$ for rabbits, $P = 0.372$ for pigs (fig. S4)]. Similarly, S-HDL did not significantly affect cellular proliferative activity in the vessel wall as assessed by PET imaging of ^{18}F-FLT uptake (Fig. 3C), although a trend was observed in pigs [LMM $P = 0.146$ for rabbits, $P = 0.086$ for pigs (fig. S4)], or vessel wall permeability, as measured both in vivo by DCE-MRI [Fig. 4A; LMM $P = 0.219$ for rabbits, $P = 0.292$ for pigs (fig. S4)] and ex vivo by Evans Blue NIRF imaging (Fig. 4B). In rabbits, we observed significantly reduced vessel wall area in the abdominal aortas of S-HDL–treated animals compared to controls [Fig. 4C, top; LMM $P = 0.001$ (fig. S4)], as assessed by T2-weighted MRI. In pigs, S-HDL treatment significantly halted vessel wall enlargement as compared to untreated animals [Fig. 4C, bottom; LMM $P = 0.036$ (fig. S4)]. Representative histological sections from rabbit and porcine specimens are shown in fig. S5.

Overall, in rabbits, we observed decreased imaging marker values in 74% of terminal scans with respect to baseline in the S-HDL group, whereas in the placebo group, we noted increased values in 58% of the scans (Fig. 4D). The median change between scans for the measured imaging parameters in the S-HDL group was −12.8% [interquartile range (IQR): −27.1 to 1.8%], which was significantly different from that in the placebo group (median: 6.5% [IQR: −14.3 to 23.4 %], $P = 0.011$; Fig. 4E). Similarly, in pigs, we observed elevated imaging marker values in 69% of terminal scans compared to baseline in the placebo group, with exactly the same proportion of scans showing decreased values in the S-HDL group (Fig. 4F). The variation in the monitored imaging markers was significantly different between groups (median placebo: 12.1 % [IQR: −3.9 to 28.0 %] versus median S-HDL: −7.7% [IQR: −22.5 to 0.9 %], $P = 0.014$; Fig. 4G). A combined representation of the variation in all imaging markers as a result of treatment in individual rabbits and pigs can be found in fig. S6.

S-HDL toxicity evaluation in pigs

Blood samples from pigs in both treatment groups were collected at the end of the study and analyzed for general biochemistry (Table 1) and complete blood count (Table 2) analysis. Liver enzymes [alkaline phosphatase (ALP), alanine aminotransferase (ALT), aspartate aminotransferase (AST), and gamma-glutamyl transferase (GGT)] and bilirubin concentrations were unaffected by S-HDL treatment. S-HDL treatment did not affect blood cholesterol concentration ($P = 0.80$), confirming that S-HDL's effects are independent of simvastatin's cholesterol-lowering properties. The other analyzed parameters had no significant differences between the two groups except for decreased blood glucose concentration in the S-HDL–treated animals ($P = 0.03$). Complete blood count results showed no difference in red blood cell, white blood cell, neutrophil, lymphocyte, or monocyte numbers. However, the neutrophil compartment was reduced ($P = 0.03$), whereas the lymphocyte compartment expanded ($P = 0.03$) in S-HDL–treated animals compared to controls. Together, these data demonstrate that 2 weeks of S-HDL nanoimmunotherapy had rapid effects on different atherosclerosis-related parameters without measurable toxicity in a large animal model.

DISCUSSION

A record of more than 1500 nanomedicine-related studies were published in 2018, according to the Web of Science. However, until late 2017, only 50 nanodrugs were available for clinical use in the United States (13). When nanoformulations reach late clinical trial phases, the vast majority of them fail to show their purported advantages over the free drug and, hence, any additional benefit to patients. This abysmal gap between preclinical nanomedicine and clinical application reflects the numerous translational challenges facing the field. Although many factors likely contribute to this gap, oftentimes, translation fails because of a lack of appropriate evaluation before moving to humans. Here, we report the translational workflow that we developed to escalate a nanoimmunotherapy from evaluation in mouse models to large rabbit and porcine atherosclerosis models.

In our quest to translate our S-HDL nanoimmunotherapy, we first faced the need to produce bulk amounts of nanoimmunotherapeutic to treat large animals. We handled this issue by developing and implementing a new scaled-up microfluidizer-based method that affords an 80-fold higher production rate. The resulting material had physicochemical properties similar to the traditionally produced
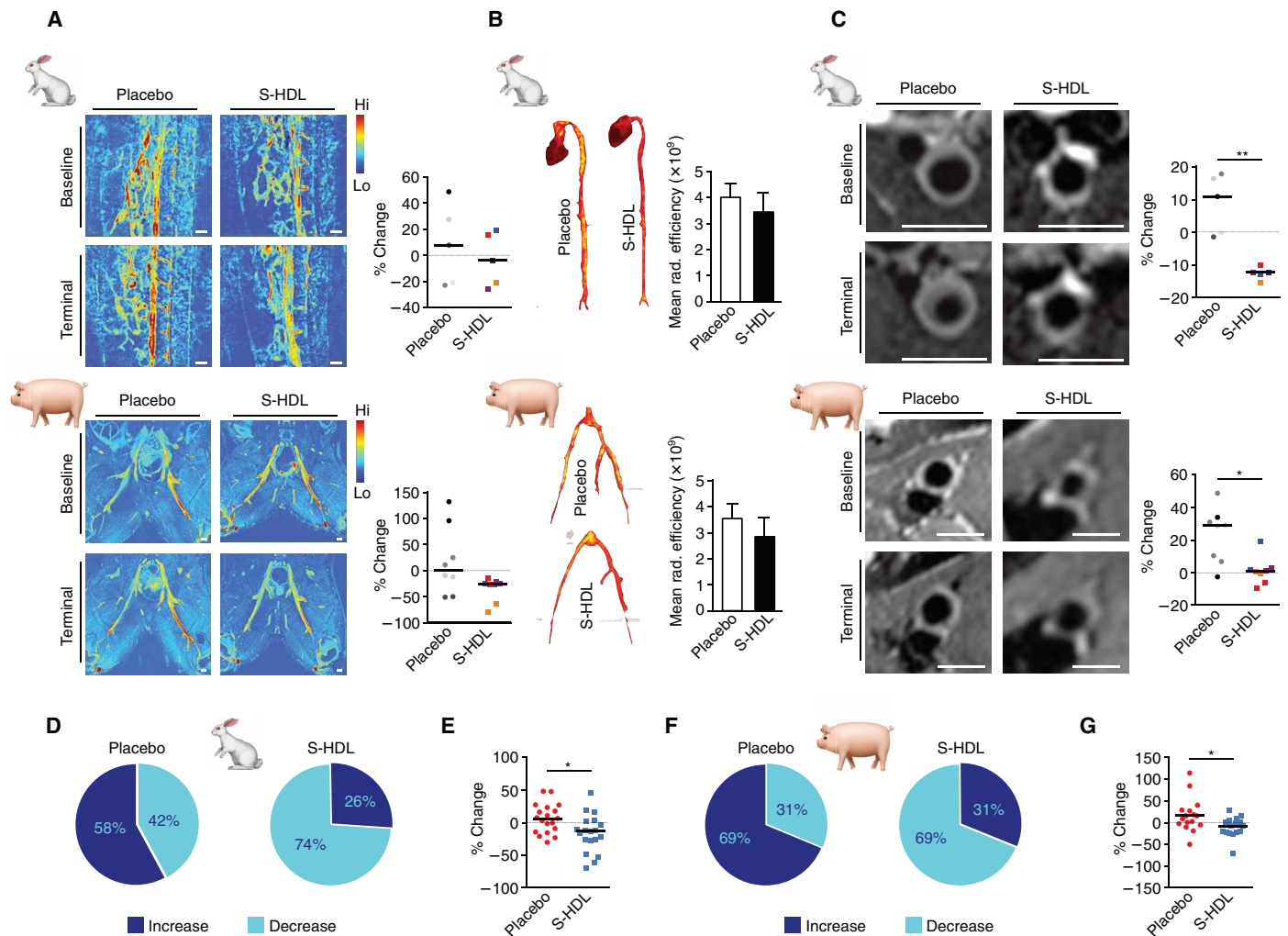
Fig. 4. Imaging-guided S-HDL nanoimmunotherapy in rabbits and pigs: MRI-based readouts. (**A**) 3D dynamic contrast–enhanced MRI-based vessel wall permeability measurements in rabbits ($n = 5$ per group; top) and pigs ($n = 4$ per group; bottom) treated with PBS (placebo) or S-HDL. Scale bars, 10 mm. (**B**) Ex vivo vessel wall permeability assessed by Evans Blue NIRF imaging in rabbit aortas and porcine femoral arteries. Data are presented as means ± SD from one experiment. (**C**) T2-weighted MRI-based vessel wall area measurements in rabbits ($n = 5$ per group; top) and pigs ($n = 4$ per group; bottom) treated with PBS (placebo) or S-HDL. Scale bars, 10 mm. In (A) and (C), dots are color-coded for individual animals, and two data points are represented per pig, corresponding to values obtained from analysis of each of the femoral arteries. Line is situated at median. (**D**) Proportion of scans that afforded increased or decreased imaging marker values in rabbits treated with PBS (placebo) or S-HDL. (**E**) Pooled representation of the variation in the four independent imaging parameters in rabbits treated with PBS (placebo) or S-HDL (line is situated at median). (**F**) Proportion of scans that afforded increased or decreased imaging marker values in pigs treated with PBS (placebo) or S-HDL. (**G**) Pooled representation of the variation in the four independent imaging parameters in pigs treated with PBS (placebo) or S-HDL (line is situated at median). Results shown in (A) and (C) were obtained in one experiment and analyzed using a linear mixed model (see the "Statistical analysis" section for details), whereas results shown in (B), (E), and (G) were analyzed using the Mann-Whitney test. *$P < 0.05$ and **$P < 0.01$.

nanoimmunotherapy. The scaled-up nanoimmunotherapeutic's in vivo behavior, including its biodistribution, pharmacokinetic profile, ability to reach the plaque, cellular specificity, and therapeutic efficacy, was comparable to our previous observations using benchtop-produced S-HDL.

Noninvasive imaging can probe molecular processes in vivo and is therefore a very powerful tool for evaluating new therapies. Imaging is increasingly integrated in clinical trials to provide surrogate end points of treatment response without the need for long follow-up periods or large patient cohorts (*14*). We used imaging at two different stages in the translational workflow. First, we conducted a quantitative in vivo performance evaluation using a radiolabeled analog of

the nanoimmunotherapy, which allowed us to verify plaque accumulation and visualize overall biodistribution. Second, we developed a multiparametric imaging protocol to quantify the effect of nanoimmunotherapy on several disease markers. The complexity of the atherosclerotic process mandates the use of a multimodal approach, allowing assessment of plaque morphology and activity to better characterize lesions. PET/MRI is very well suited to this task because it combines MRI's excellent soft tissue contrast and spatial resolution with PET's high sensitivity and the specificity of the radiotracers. Despite the treatment's short duration, our results show a trend toward reduction in evaluated atherosclerosis burden parameters, including vessel wall thickness and permeability,

Table 1. Blood biochemistry results from pigs with atherosclerosis treated with PBS (placebo) or S-HDL. Data are presented as median [interquartile range]. Bolded values indicate $P < 0.05$. ALP, alkaline phosphatase; SGPT, serum glutamic pyruvic transaminase; ALT, alanine aminotransferase; SGOT, serum glutamic-oxaloacetic transaminase; GGT, gamma-glutamyl transferase; AST, aspartate aminotransferase; CPK, creatine phosphokinase; BUN, blood urea nitrogen.

	Placebo	S-HDL	P
ALP (U/liter)	127 [87–175]	85 [70–132]	0.15
SGPT (ALT) (U/liter)	45 [39–67]	51 [38–65]	0.94
SGOT (AST) (U/liter)	69 [43–222]	67 [53–160]	0.80
GGT (U/liter)	40 [34–78]	41 [39–56]	0.67
CPK (U/liter)	740 [406–1817]	796 [431–1024]	0.94
Total bilirubin (mg/dl)	0.2 [0.1–0.2]	0.2 [0.2–0.3]	0.28
Direct bilirubin (mg/dl)	0.0 [0.0–0.1]	0.0 [0.0–0.1]	>0.99
Indirect bilirubin (mg/dl)	0.1 [0.1–0.2]	0.2 [0.1–0.3]	0.37
Total protein (g/dl)	6.6 [5.9–6.7]	6.8 [6.5–7.1]	0.21
Albumin (g/dl)	3.5 [3.4–4.0]	4.0 [3.7–4.5]	0.29
Globulin (g/dl)	2.6 [2.5–3.1]	2.8 [2.5–2.9]	0.81
Albumin/ globulin ratio	1.4 [1.2–1.6]	1.4 [1.3–1.8]	0.75
BUN (mg/dl)	12 [10–14]	10 [8.5–17]	0.79
Creatinine (mg/dl)	0.9 [0.8–1.2]	1.0 [0.9–1.2]	0.69
BUN/creatinine ratio	13 [9.1–17]	11 [9.0–15]	0.94
Glucose (mg/dl)	76 [71–80]	67 [34–69]	**0.03**
Cholesterol (mg/dl)	573 [450–628]	507 [426–747]	0.80
Triglycerides (mg/dl)	62 [26–72]	72 [48–186]	0.31
Sodium (mM)	140 [140–141]	139 [136–141]	0.20
Potassium (mM)	4.4 [4.3–5.1]	4.6 [4.1–7.5]	0.44
Na/K ratio	32 [28–33]	30 [21–35]	0.44
Magnesium (mg/dl)	2.0 [1.9–2.4]	2.1 [1.9–2.8]	0.81
Calcium (mg/dl)	10 [9.4–11]	10 [9.9–10.2]	0.88
Phosphorus (mg/dl)	7.4 [7.2–7.9]	6.9 [6.4–8.6]	0.53
Bicarbonate (mM)	22 [19–24]	19 [17–24]	0.49
Chloride (mM)	99 [98–101]	102 [97–105]	0.49

Table 2. Complete blood count results from pigs with atherosclerosis treated with PBS (placebo) or S-HDL. Data are presented as median [interquartile range]. Bolded values indicate $P < 0.05$. MCV, mean corpuscular volume; MCH, mean corpuscular hemoglobin.

	Placebo	S-HDL	P
Red blood cell # (M/μl)	8.1 [6.3–9.7]	5.0 [3.8–6.5]	0.06
Hemoglobin (g/dl)	13 [10–16]	8.9 [7.3–11]	0.19
Hematocrit (%)	43 [32–54]	31 [25–45]	0.29
MCV (fl)	53 [51–56]	66 [62–69]	**0.02**
MCH (pg)	16 [16–17]	18 [17–19]	**0.03**
MCH concentration (g/dl)	30 [29–31]	28 [26–30]	0.11
Reticulocyte # (K/μl)	27 [20–42]	65 [38–161]	0.06
Reticulocyte (%)	0.28 [0.25–0.60]	1.5 [0.7–3.2]	0.06
Platelet # (K/μl)	175 [142–193]	226 [166–393]	0.19
White blood cell # (K/μl)	6.9 [5.5–9.6]	5.5 [5.2–5.9]	0.25
Neutrophil # (K/μl)	3.3 [2.4–5.2]	1.6 [1.1–2.1]	0.06
Lymphocyte # (K/μl)	3.4 [2.8–3.8]	3.8 [3.1–4.1]	0.68
Monocyte # (K/μl)	0.35 [0.24–0.49]	0.24 [0.17–0.36]	0.26
Eosinophil # (K/μl)	0.08 [0.05–0.16]	0.03 [0.02–0.12]	0.44
Basophil # (K/μl)	0.0 [0.0–0.01]	0.01 [0.0–0.01]	0.52
Neutrophil (%)	51 [41–56]	33 [20–37]	**0.03**
Lymphocyte (%)	41 [39–52]	63 [59–72]	**0.03**
Monocyte (%)	4.4 [3.8–5.9]	4.3 [3.1–6.3]	0.71
Eosinophil (%)	1.0 [0.6–2.1]	0.5 [0.3–2.0]	0.44
Basophil (%)	0.0 [0.0–0.1]	0.2 [0.0–0.2]	0.29

inflammation, and proliferation. This latter outcome seems to mirror our observations from previous studies because S-HDL nano-immunotherapy exerts its effects through macrophage proliferation inhibition (7), which is a dominant process in plaque inflammation in advanced atherosclerosis. As previously observed in our mouse studies (6, 7, 9), these anti-atherosclerosis effects were independent of simvastatin's cholesterol-lowering properties. This is likely due to S-HDL's targeting properties upon intravenous administration, which results in plaque macrophage delivery and diminishes simvastatin exposure to hepatocytes as compared to oral administration (15). In addition, the short treatment duration may also have contributed to stable lipid concentrations.

Translating nanotherapy from small to large animal models is challenging for various reasons. One of those challenges is the restraint on group sizes typically associated with large animal studies, due to cost, logistical, and ethical reasons. Here, we applied the concept of triangulation by taking the convergence of measurements from distinct imaging modalities and different animal models (mice, rabbits, and pigs) to help increase confidence that an observed effect is correctly identified. This integrative analysis provides an overall picture of treatment effect on an intrinsically multifaceted disease such as atherosclerosis and substantially increases the relevance of the results while using restricted group sizes.

The use of HDL nanobiologics as myeloid cell–specific therapies is a promising treatment avenue for many immune-related diseases. One of the biggest hurdles for clinically translating these nano-immunotherapies will be implementing large-scale APOA1 extraction/ production methods. In this study, we optimized a high-throughput method to isolate APOA1 through purification and delipidation of human HDL. Although this is a convenient way to extract the protein,

Binderup *et al.*, *Sci. Transl. Med.* **11**, eaaw7736 (2019)   21 August 2019

8 of 13

safety concerns regarding sterility and risk of contamination would need to be addressed. Alternatively, APOA1 can be produced recombinantly in bacteria or mammalian cells, but production and purification processes in this case can be troublesome and result in low yields.

Another pivotal issue in developing and translating these nano-immunotherapies is assessing their safety. Simvastatin can have deleterious effects on the liver and muscles, especially with higher doses. Yet our nanoimmunotherapy's uptake in muscle was low. Blood biochemistry analysis revealed no difference in creatine phosphokinase, indicating that our treatment had no harmful effect on myocytes. In contrast to muscle tissue, our nanoimmunotherapy is taken up by the liver in high quantities, as shown by the biodistribution data. Therefore, it is vital to evaluate signs of liver toxicity. In previous mouse studies, we observed neither metabolic changes nor signs of liver toxicity (9). Our current study confirms this point because transaminases (ALT and AST), ALP, and bilirubin concentrations were unaffected. Effects on the immune system must also be investigated. We observed no changes in white blood cell count or in lymphocyte, neutrophil, and monocyte numbers, although a rebalancing in the lymphocyte and neutrophil compartments was detected.

The promising results that we obtained in large animals are encouraging and may represent a therapeutic option for acutely treating atherosclerosis-related inflammation. This option has clinically relevant value after an acute cardiovascular event such as myocardial infarction or stroke. These events are known to exacerbate inflammation and thus aggravate ongoing atherosclerosis, leading to a high recurrence rate of acute events in these patients. Thus, it is conceivable that an intervention with our nanoimmunotherapy after a cardiovascular event could be beneficial by rapidly suppressing the exaggerated inflammatory activity in atherosclerotic lesions during that critical period (16).

Our study has limitations. First, owing to logistical considerations, the number of large animals was limited. A total of six pigs were used to develop the imaging protocols, plus another 12 for the biodistribution and efficacy studies. For symmetry, we used the same number of rabbits. These restricted group sizes hampered statistical power of individual marker measurements. However, implementing a longitudinal multiplex imaging-based therapy monitoring approach allowed us to measure treatment response in individual animals from different angles and thus obtain meaningful results on the therapy's effect on overall disease burden. Second, using ^{18}F FDG as an imaging marker of inflammation may also have certain limitations in large plaques because hypoxia-induced uptake may be predominant (17). This could have masked the anti-inflammatory effects of S-HDL to a certain degree.

In conclusion, we presented the production scaling and imaging-facilitated development workflow for evaluating a nanoimmunotherapeutic. In the context of cardiovascular disease, we showed that our nanoimmunotherapeutic's anti-atherosclerotic effects in mice were maintained in large animals. We anticipate increased potential for nanomedicines as immunotherapeutics and demonstrate the value of—and need for—noninvasive imaging readouts when evaluating such nanoimmunotherapies in large animal disease models.

MATERIALS AND METHODS
Study design
The goal of this study was to develop translational methods for the scale-up and evaluation of our nanoimmunotherapy. The scaled-up S-HDL nanoformulation, produced by high-pressure microfluidizer homogenization, was first validated in the $Apoe^{-/-}$ atherosclerosis mouse model, using sample sizes determined by statistical power calculations based on our previous work. Subsequently, S-HDL's in vivo behavior and therapeutic efficacy were evaluated in rabbit and swine atherosclerosis models by PET/CT and PET/MRI. Sample sizes were established by logistical and ethical reasons. Animals were randomized into a placebo group [receiving phosphate-buffered saline (PBS) injections] and an S-HDL nanoimmunotherapy treatment group. Two pigs, one from each group, had to be excluded from imaging analysis. One of them suffered a thrombotic incident, whereas, for the other animal, data from two imaging sessions were irrecoverably lost because of technical issues with acquisition. Toxicology data were collected for all pigs and included in the analysis. Imaging data were reconstructed and analyzed in a blinded fashion when all scans had been completed.

Materials
Phospholipids [DMPC (1,2-dimyristoyl-sn-glycero-3-phosphatidylcholine), MHPC (1-myristoyl-2-hydroxy-sn-glycero-phosphocholine), and DSPE (1,2-distearoyl-sn-glycero-3-phosphoethanolamine)] and simvastatin were purchased from Avanti Polar Lipids and AK Scientific, respectively. All other chemicals were acquired from Sigma-Aldrich. APOA1 was isolated from human HDL concentrates (Bioresource Technology) following a previously described procedure (18). [89]Zr was produced at Memorial Sloan Kettering Cancer Center on an EBCO TR19/9 variable beam energy cyclotron (Ebco Industries Inc.) via the $^{89}Y(p,n)^{89}Zr$ reaction and purified in accordance with previously reported methods (19). [18]F was produced via the $^{18}O(p,n)^{18}F$ reaction using a GEMS PETtrace 800 cyclotron (GE Healthcare).

Radiotracers
^{18}F-FDG was purchased from NCM USA, whereas ^{18}F-FLT was synthesized in-house by adapting already published procedures (20, 21). Briefly, a QMA cartridge containing cyclotron-produced [^{18}F]fluoride was eluted with a solution containing 9 mg of 4,7,13,16,21,24-hexaoxa-1,10-diazabicyclo[8.8.8]hexacosane (Kryptofix [2.2.2]), 0.08 ml of 0.15 M K_2CO_3, and 1.92 ml of acetonitrile into a 5-ml reaction vial. Solvents were removed azeotropically at 120°C under a slight flow of nitrogen. Then, 5 mg of precursor 3-N-Boc-5′-O-dimethoxytrityl-3′-O-nosyl-thymidine (6.02 μmol; ABX) in 500 μl of dry acetonitrile was added, and the reaction mixture was heated to 150°C for 10 min. After cooling to room temperature, 1 N hydrochloric acid (400 μl) was added, and the mixture was heated to 90°C for 10 min. The reaction mixture was finally quenched by adding 2 M sodium acetate solution (1.3 ml) and purified by high-performance liquid chromatography (HPLC) to yield pure ^{18}F-FLT using a C18 semi-preparative column (250 mm by 10 mm, 5 μm; Luna C18, Phenomenex) and isocratic elution with 8% EtOH/92% water at a flow rate of 5.5 ml/min (retention time, ~16 min). Purity was assessed via Radio-HPLC using a C18 analytical column (100 Å, 250 mm by 4.6 mm, 5 μm; Atlantis T3, Waters) and isocratic elution with 10% EtOH/90% water at a flow rate of 1 ml/min (RT = 7.4 min).

Animals
Female $Apoe^{-/-}$ and C57BL/6 mice were purchased from the Jackson Laboratories. Male New Zealand white rabbits (n = 12) and familial hypercholesterolemia pigs (n = 11; 4 males and 7 females) were acquired from Charles River Laboratories and University of Wisconsin,

Binderup et al., Sci. Transl. Med. 11, eaaw7736 (2019)   21 August 2019

9 of 13

respectively. All animal experiments were performed in accordance with protocols approved by the Institutional Animal Care and Use Committees of Mount Sinai, the Memorial Sloan Kettering Cancer Center, and/or the Skirball Center for Cardiovascular Research and followed the National Institutes of Health guidelines for animal welfare.

Mouse model of atherosclerosis

Female $Apoe^{-/-}$ mice (B6.129P2-Apoe[tm1Unc/J], 4 to 6 weeks old) were fed a high-fat diet (Harlan Teklad TD.88137, 42% calories from fat; Envigo) for 12 weeks. Under these conditions, this animal model develops atherosclerotic lesions due to high low-density lipoprotein cholesterol concentrations in blood resulting from their lack of apolipoprotein E (22, 23).

Rabbit model of atherosclerosis

Model was based on prior work (24, 25). Male CRL SPF New Zealand white rabbits (2.5 to 3 months old) underwent double balloon injury of the thoracic and abdominal aorta to induce atherosclerosis. Denudation was performed by introducing a 4F-Fogarty embolectomy catheter (Edwards Lifesciences) through the femoral artery and by inflating the balloon to 2 atm under fluoroscopic guidance. The procedure was repeated on the contralateral extremity 4 weeks later. Surgery was performed under anesthesia with intramuscular ketamine (35 mg/kg) and xylazine (5 mg/kg). To further accelerate plaque progression, animals were fed a high-cholesterol diet (Research Diets) enriched initially with 0.3% cholesterol for 8 weeks and, subsequently, 0.15% for at least 8 weeks.

Porcine model of atherosclerosis

Model was based on prior work (26). We used the familial hypercholesterolemia swine model of atherosclerosis. Because of a mutation in Lpb5 at the apolipoprotein B locus, these animals carry a liver low-density lipoprotein receptor deficiency that results in hypercholesterolemia and atherosclerosis. To accelerate plaque development, animals were fed a high-fat diet (enriched with 2% cholesterol) for 12 weeks, and balloon injuries were performed in the deep and superficial femoral arteries on both legs with access through the carotid artery with a 4F-Fogarty embolectomy catheter (Edwards Lifesciences).

Synthesis of S-HDL by high-pressure microfluidic homogenization

Simvastatin and phospholipids MHPC and DMPC were mixed (1.79:1:10 mass ratio) in 4:1 chloroform/methanol in a 2-liter round-bottom flask. A lipid film was formed by reduced-pressure rotary evaporation removal of solvents (table S1). The resulting film was further dried under a nitrogen flow for 1 hour. A solution of APOA1 was added, followed by PBS to reach a volume of about 0.5 liters. The film was left to hydrate at 37°C using a rotary evaporator to facilitate mixing. In batches of 0.25 liters, the crude suspension underwent high-pressure microfluidics homogenization using a microfluidizer 110-S (Microfluidics). The solution was pressurized at 120 psi to pass through the microfluidics chamber, which was refrigerated with an ice-water bath, 8 to 12 times. The resulting solution was left overnight at room temperature and then centrifuged at 4000 rpm for 1 hour at 4°C. The supernatant was then passed through the 0.2-μm Stericup Vacuum Filter Unit (MilliporeSigma) and subsequently concentrated and washed twice with PBS using a 100-kDa Vivaflow device (Sartorius). After the final concentration round, the final volume was ~0.1 liters.

Samples were left overnight at 4°C and then centrifuged at 4000 rpm for 1 hour at 4°C. Last, the supernatant was passed through the 0.2-μm Stericup Vacuum Filter Unit (MilliporeSigma) under clean, sterile conditions and kept at 4°C until use. Because of simvastatin's sensitivity to light, samples were protected from light during the entire formulation process.

S-HDL quality control

Size, dispersity, and simvastatin concentration were measured for every S-HDL batch to assess the production quality. Size and dispersity were determined immediately after homogenization and at the end of the purification/sterilization process by dynamic light scattering, using a ZetaPALS analyzer (Brookhaven Instruments Corporation). Simvastatin concentration was measured by HPLC using a previously described method (27). Briefly, an aliquot of S-HDL (100 μl) formulation was dried for 18 hours in a desiccator and then solubilized in acetonitrile (1 ml) and sonicated for 30 min on ice. After centrifugation (14,000g for 10 min), supernatants were analyzed by reverse-phase HPLC using an Ascentis C18 column (100 mm by 4.6 mm, 3-μm particles) using 80:20 acetonitrile/water as eluent. Simvastatin absorption was quantified at 238 nm.

Evaluation of S-HDL treatment efficacy in mice

Female $Apoe^{-/-}$ mice ($n = 24$, 12 weeks on Western diet; weight, 29.6 ± 4.1 g) were randomized into two groups of 12 animals each, receiving (i) PBS or (ii) S-HDL at a simvastatin dose of 60 mg/kg of body weight. Nanobiologic doses and PBS were administered via a lateral tail vein. Treatment consisted of four administrations, one every 48 hours. Twenty-four hours after the last dose, animals were euthanized and extensively perfused with saline, and the aortas were carefully excised for ex vivo evaluation by flow cytometry ($n = 10$) and histological analysis ($n = 2$).

Flow cytometry

The aorta, from aortic root to the iliac bifurcation, was gently cleaned of fat, collected, and then digested using an enzymatic digestion solution containing Liberase TH (4 U/ml; Roche, Basel, Switzerland), deoxyribonuclease I (40 U/ml; Sigma-Aldrich), and hyaluronidase (60 U/ml; Sigma-Aldrich) in PBS at 37°C for 60 min. Cells were filtered through a 70-μm cell strainer and washed with serum-containing media. Spleens were mashed, filtered through a 70-μm cell strainer, incubated with lysis buffer for 4 min, and washed with serum-containing media. Single cell suspensions were stained with the following monoclonal antibodies: anti-CD11b (clone M1/70; no. 101228, BioLegend), anti-F4/80 (clone BM8; no. 123114, BioLegend), anti-CD11c (clone N418; no. 117310, BioLegend), anti-CD45 (clone 30-F11; no. 103138, BioLegend), anti-Ly6C (clone AL-21; no. 560592, BD Biosciences), and a lineage cocktail (Lin) containing anti-CD90.2 (clone 53-2.1; no. 48-0902-82, eBioScience), anti-Ter119 (clone TER119; no. 48-5921-82, eBioScience), anti-NK1.1 (clone PK136; no. 48-5941-82, eBioScience), anti-CD49b (clone DX; no. 48-5971-82, eBioScience), anti-CD45R (clone RA3-6B2; no. 48-0452-82, eBioScience), and anti-Ly6G (clone 1A8; no. 127612, BioLegend). Macrophages were identified as $CD45^+$, $CD11b^{hi}$, $Lin^{-/lo}$, $CD11c^{lo}$, and $F4/80^{hi}$. $Ly6C^{hi}$ monocytes were identified as $CD45^+$, $CD11b^{hi}$, $Lin^{-/lo}$, $CD11c^{lo}$, and $Ly6C^{hi}$. Data were acquired on an LSR II and an LSRFortessa flow cytometer (BD Biosciences), and DiO signal was recorded in the fluorescein isothiocyanate (FITC) channel. The data were analyzed using FlowJo v10.0.7 (Tree Star).

Binderup et al., Sci. Transl. Med. 11, eaaw7736 (2019)   21 August 2019

10 of 13

Radiolabeling of S-HDL

DFO functionalized S-HDL was prepared following a previously described procedure (10) by adding 0.7 weight % of the phospholipid chelator DSPE-DFO (28) to the lipid mix at the expense of DMPC. The resulting nanoparticles were radiolabeled following a previously reported method (10). Briefly, DFO-bearing S-HDL was reacted with ^{89}Zr-oxalate at an APOA1 ratio of ~37 MBq/mg in PBS (pH 6.8 to 7.1) at 37°C for 2 hours. [^{89}Zr]-S-HDL was purified by centrifugal filtration using 10-kDa molecular weight cutoff Visvaspin tubes. Radiochemically pure [^{89}Zr]-S-HDL was mixed with unlabeled S-HDL to achieve the desired simvastatin dose, and the mixture was allowed to equilibrate for at least 4 hours.

PET/CT imaging, biodistribution, and pharmacokinetics in mice

$Apoe^{-/-}$ mice ($n = 4$; 12 weeks on high-fat diet) were injected with [^{89}Zr]-S-HDL (7.0 ± 1.1 MBq; simvastatin, 60 mg/kg) in 150 to 200 μl of PBS solution via the lateral tail vein. At 2 and 30 min and 2, 6, and 18 hours, blood (5 to 10 μl) was sampled from the tail vein and weighed. Radioactivity content was measured using a Wizard^2 2480 automatic gamma counter (Perkin Elmer). At 24 hours after administration, animals were anesthetized with isoflurane (Baxter Healthcare)/oxygen gas mixture (2% for induction and 1% for maintenance), and a scan was then performed using an Inveon PET/CT scanner (Siemens Healthcare Global). Whole-body PET static scans recording a minimum of 30 million coincident events were performed, with duration of about 20 min. The energy and coincidence timing windows were 350 to 700 keV and 6 ns, respectively. The image data were normalized to correct for nonuniform PET response, dead-time count losses, positron branching ratio, and physical decay to the time of injection, but no attenuation, scatter, or partial-volume averaging correction was applied. Whole-body standard low-magnification CT scans were performed with the following acquisition parameters: voltage of 80 kV, current of 500 μA, exposure time of 145 ms per frame, and 120 rotational steps for a total of 220°.

After the scan, at 26 hours after injection, animals were euthanized and perfused with PBS. Tissues of interest (blood, kidneys, liver, spleen, lungs, heart, brain, aorta, and muscle) were collected, blotted, and weighed before radioactivity counting on a Wizard^2 2480 automatic gamma counter. Radioactivity values were corrected for decay and normalized to tissue weight to express radioactivity concentration as percentage injected dose per gram (%ID/g).

[^{89}Zr]-S-HDL PET imaging, biodistribution, and plaque targeting in rabbits and pigs

[^{89}Zr]-S-HDL was administered via the ear vein to atherosclerotic rabbits ($n = 2$; 20.4 ± 3.1 MBq; simvastatin, 15 mg/kg) and pigs ($n = 2$; 142.4 ± 18.3 MBq; simvastatin, 7.5 mg/kg) while anesthetized on the bed of a Siemens Biograph mCT PET/CT TOF scanner. For the CT scan, iodine contrast (76% Iopamidol injection, Bracco Diagnostics) was injected in rabbits (10 ml, 1 ml/s, no delay) and pigs (70 ml, 1 ml/s, 6-s delay). Whole-body static scans were acquired 0.5, 24, and 48 hours after injection. Before PET acquisition, a CT scan was recorded with the following parameters: voltage of 140 kVp, tube current of 34 mA, exposure time of 1000 ms, and slice thickness of 1 mm. The CT scan was used for attenuation correction of the PET data.

In addition to biodistribution imaging by PET/CT, the ability of the nanoimmunotherapeutic to reach and accumulate in athero-sclerotic plaques was imaged in vivo using PET/MRI. After the 48-hour PET/CT scan, animals were transferred to a Siemens Biograph mMR 3T PET/MRI scanner and imaged using a body matrix coil. After scout scans, a bright-blood, 3D TOF noncontrast-enhanced angiography sequence was acquired to better localize arterial anatomical landmarks (rabbits: renal arteries and iliac bifurcation, pigs: superficial femoral arteries). Imaging parameters for the rabbit protocol were as follows: TR, 23 ms; TE, 2.83 ms; flip angle, 20°; spatial resolution, 0.7 mm by 0.7 mm by 1 mm; acquisition plane, axial; number of slices, 200; and number of signal averages, 1; the parameters for the pig protocol were as follows: TR, 23 ms; TE, 3.69 ms; flip angle, 20°; spatial resolution, 1.4 mm by 1.4 mm by 1.5 mm; acquisition plane, axial; number of slices, 228; and number of signal averages, 1. Subsequently, the PET scan was initiated simultaneously with a black-blood, 3D T2-weighted SPACE (sampling perfection with application-optimized contrasts using different flip angle evolution) sequence acquired for vessel wall delineation, with the following imaging parameters for rabbits: TR, 1600 ms; TE, 115 ms; spatial resolution, 0.63 mm by 0.63 mm by 0.63 mm; acquisition plane, sagittal; number of slices, 30; and number of signal averages, 4; the parameters for pigs were as follows: TR, 1200 ms; TE, 112 ms; spatial resolution, 0.63 mm by 0.63 mm by 0.63 mm; acquisition plane, coronal; number of slices, 144; and number of signal averages, 4. Attenuation correction of PET images was performed using the built-in MR-based attenuation correction map, obtained from a two-point Dixon sequence allowing for fat/water separation. Rabbit attenuation maps were segmented into two compartments (soft tissue and air), whereas pig attenuation maps were segmented into four compartments (soft tissue, fat, air, and lungs).

Shortly after the last scan, animals were euthanized, rabbits were thoroughly perfused with isotonic saline, and tissues of interest (liver, spleen, kidney, lung, and muscle), as well as arteries of interest, were collected for ex vivo radioactivity quantification, as described above, NIRF imaging, and autoradiography. In both cases, PET images were reconstructed using the ordinary Poisson ordered subset expectation-maximization algorithm with point-spread function correction. Image analysis was conducted using the OsiriX Imaging Software by drawing regions of interest (ROIs) on the selected tissues (liver, kidneys, and spleen for both rabbits and pigs, as well as abdominal aorta—from renal artery to iliac bifurcation—and super-ficial femoral arteries for rabbits and pigs, respectively). Blood activity was quantified in the left ventricle. Standardized uptake values (SUVs; defined as [pixel value (Bq/ml) × weight of the subject (kg)/dose (Bq)] × 1000 g/kg) were obtained by averaging SUV_{mean} or SUV_{max} values in each ROI drawn on at least five slices of the organ of interest and on all slices of the abdominal aorta (rabbits) and superficial femoral arteries (pigs). Maximal target-to-background (TBR_{max}) values were calculated by dividing average SUV_{max} from the abdominal aorta (rabbits) and superficial femoral arteries (pigs) by average SUV_{max} from muscle in the same animal.

Evaluation of S-HDL treatment efficacy in rabbits and pigs

Rabbits ($n = 10$; weight, 3.5 ± 0.3 kg) and pigs ($n = 10$; weight, 31.2 ± 5.7 kg) with atherosclerosis were randomized into two groups of five animals, receiving either PBS or S-HDL. The simvastatin dose was 15 and 7.5 mg/kg for rabbits and pigs, respectively. Treatment consisted of four intravenous injections, one every 4 days. Response was evaluated noninvasively and longitudinally using a multi-parametric PET/MRI protocol (see below). Shortly after the last

scan and 30 min before euthanasia, Evans Blue was injected intravenously for ex vivo assessment of vessel wall permeability. Immediately after euthanasia, animals were perfused with isotonic saline, and tissues of interest (aorta for rabbits and femoral tree for pigs) were collected for ex vivo evaluation by NIRF imaging and histological analysis. The femoral tree was thoroughly rinsed in isotonic saline once harvested.

Noninvasive PET/MRI evaluation of S-HDL treatment response in rabbits and pigs

A multiparametric PET/MRI protocol was implemented to monitor treatment. Twenty-four hours before the first injection, animals underwent a PET/MRI session consisting of ^{18}F-FDG–based assessment of plaque inflammation and 3D anatomical MRI using the 3D T2-weighted SPACE sequence described above. The next day, animals had a second PET/MRI session to determine plaque macrophage proliferation with ^{18}F-FLT and vessel wall permeability by 3D DCE-MRI. DCE-MRI was performed using a 3D MERGE (motion-sensitized driven equilibrium prepared rapid gradient echo) sequence to simultaneously achieve blood pool signal suppression and signal enhancement in atherosclerotic plaques. 3D DCE-MRI parameters in rabbits were as follows: TR, 491.08 ms; TE, 5.32 ms; flip angle, 20°; spatial resolution, 0.63 mm by 0.63 mm by 0.63 mm; acquisition plane, sagittal; number of slices, 20; number of dynamics, 20; number of signal averages, 1; and temporal resolution, 31 s; the parameters for pigs were as follows: TR, 1106.1 ms; TE, 4.3 ms; flip angle 20°; spatial resolution, 0.63 mm by 0.63 mm by 0.63 mm; acquisition plane, coronal; number of slices, 40; number of dynamics, 12; number of signal averages, 1; and temporal resolution, 101 s. Dynamic images were acquired before, during, and after the injection of gadolinium–diethylenetriamine penta-acetic acid (Gd-DTPA) (0.2 mmol/kg; Magnevist, Bayer). The same imaging sessions were performed at the end of treatment, on days 14 and 15 after the first injection. Radiotracers ^{18}F-FDG (rabbits$_{baseline}$: 118.4 ± 17.4 MBq, $n = 10$; rabbits$_{terminal}$: 121.4 ± 16.4 MBq, $n = 10$; pigs$_{baseline}$: 260.3 ± 14.7 MBq, $n = 10$; pigs$_{terminal}$: 269.5 ± 32.8 MBq, $n = 10$) and ^{18}F-FLT (rabbits$_{baseline}$: 108.8 ± 24.5 MBq, $n = 10$; rabbits$_{terminal}$: 119.4 ± 12.2 MBq, $n = 10$; pigs$_{baseline}$: 230.2 ± 34.0 MBq, $n = 10$; pigs$_{terminal}$: 201.7 ± 54.1 MBq, $n = 10$) were administered via the ear vein. For ^{18}F-FDG imaging, animals were fasted for at least 6 hours before the scan, which was performed 2.5 hours (rabbits) and 1 hour (pigs) after administration. ^{18}F-FLT PET scans were performed 2 hours (rabbits) and 1 hour (pigs) after injection, with acquisition times of 30 min for each tracer. Both PET imaging sessions were performed on a Siemens mMR 3T PET/MRI scanner using a body matrix coil.

Statistical analysis

Data are presented as means ± SD, unless otherwise stated. Mann-Whitney tests were used to assess differences between two groups, whereas nonparametric one-way analysis of variance (ANOVA) (Kruskal-Wallis test) with multiple comparisons was used when analyzing differences between more than two groups. In the therapeutic study in rabbits and pigs, an LMM was used to statistically analyze differences in imaging-derived parameters between treatment groups. The imaging parameter at the end of the study (terminal scan) was used as the dependent variable. Type of treatment and imaging parameter at the start of the study (baseline) were defined as fixed effects, and the side (left or right femoral artery in pigs) as a random effect. For all tests, α < 0.05 represents statistical significance.

Statistical analyses were performed with GraphPad Prism, version 6.0c. Primary data are reported in data file S1.

SUPPLEMENTARY MATERIALS
stm.sciencemag.org/cgi/content/full/11/506/eaaw7736/DC1
Materials and Methods
Fig. S1. S-HDL characterization.
Fig. S2. In vivo S-HDL cell specificity evaluation.
Fig. S3. Pharmacokinetics and plaque targeting of S-HDL in rabbits and pigs.
Fig. S4. S-HDL treatment effect in rabbits and pigs.
Fig. S5. Histological evaluation of S-HDL treatment.
Fig. S6. S-HDL treatment effect in individual rabbits and pigs.
Table S1. Composition and size of different S-HDL batches prepared for this study.
Data file S1. Primary data.

REFERENCES AND NOTES

1. S. Wilhelm, A. J. Tavares, Q. Dai, S. Ohta, J. Audet, H. F. Dvorak, W. C. W. Chan, Analysis of nanoparticle delivery to tumours. *Nat. Rev. Mater.* **1**, 16014 (2016).

2. M. Lameijer, T. Binderup, M. M. T. van Leent, M. L. Senders, F. Fay, J. Malkus, B. L. Sanchez-Gaytan, A. J. P. Teunissen, N. Karakatsanis, P. Robson, X. Zhou, Y. Ye, G. Wojtkiewicz, J. Tang, T. T. P. Seijkens, J. Kroon, E. S. G. Stroes, A. Kjaer, J. Ochando, T. Reiner, C. Pérez-Medina, C. Calcagno, E. A. Fischer, B. Zhang, R. E. Temel, F. K. Swirski, M. Nahrendorf, Z. A. Fayad, E. Lutgens, W. J. M. Mulder, R. Duivenvoorden, Efficacy and safety assessment of a TRAF6-targeted nanoimmunotherapy in atherosclerotic mice and non-human primates. *Nat. Biomed. Eng.* **2**, 279–292 (2018).

3. R. Duivenvoorden, M. L. Senders, M. M. T. van Leent, C. Pérez-Medina, M. Nahrendorf, Z. A. Fayad, W. J. M. Mulder, Nanoimmunotherapy to treat ischaemic heart disease. *Nat. Rev. Cardiol.* **16**, 21–32 (2019).

4. M. S. Braza, M. M. T. van Leent, M. Lameijer, B. L. Sanchez-Gaytan, R. J. W. Arts, C. Pérez-Medina, P. Conde, M. R. Garcia, M. Gonzalez-Perez, M. Brahmachary, F. Fay, E. Kluza, S. Kossatz, R. J. Dress, F. Salem, A. Rialdi, T. Reiner, P. Boros, G. J. Strijkers, C. C. Calcagno, F. Ginhoux, I. Marazzi, E. Lutgens, G. A. F. Nicolaes, C. Weber, F. K. Swirski, M. Nahrendorf, E. A. Fisher, R. Duivenvoorden, Z. A. Fayad, M. G. Netea, W. J. M. Mulder, J. Ochando, Inhibiting inflammation with myeloid cell-specific nanobiologics promotes organ transplant acceptance. *Immunity* **49**, 819–828.e6 (2018).

5. L. Bird, Targeting trained immunity. *Nat. Rev. Immunol.* **19**, 2–3 (2019).

6. R. Duivenvoorden, J. Tang, D. P. Cormode, A. J. Mieszawska, D. Izquierdo-Garcia, C. Ozcan, M. J. Otten, N. Zaidi, M. E. Lobatto, S. M. van Rijs, B. Priem, E. L. Kuan, C. Martel, B. Hewing, H. Sager, M. Nahrendorf, G. J. Randolph, E. S. G. Stroes, V. Fuster, E. A. Fisher, Z. A. Fayad, W. J. M. Mulder, A statin-loaded reconstituted high-density lipoprotein nanoparticle inhibits atherosclerotic plaque inflammation. *Nat. Commun.* **5**, 3065 (2014).

7. J. Tang, M. E. Lobatto, L. Hassing, S. van der Staay, S. M. van Rijs, C. Calcagno, M. S. Braza, S. Baxter, F. Fay, B. L. Sanchez-Gaytan, R. Duivenvoorden, H. B. Sager, Y. M. Astudillo, W. Leong, S. Ramachandran, G. Storm, C. Pérez-Medina, T. Reiner, D. P. Cormode, G. J. Strijkers, E. S. G. Stroes, F. K. Swirski, M. Nahrendorf, E. A. Fisher, Z. A. Fayad, W. J. M. Mulder, Inhibiting macrophage proliferation suppresses atherosclerotic plaque inflammation. *Sci. Adv.* **1**, e1400223 (2015).

8. W. R. Sanhai, J. H. Sakamoto, R. Canady, M. Ferrari, Seven challenges for nanomedicine. *Nat. Nanotechnol.* **3**, 242–244 (2008).

9. A. Alaarg, M. L. Senders, A. Varela-Moreira, C. Pérez-Medina, Y. Zhao, J. Tang, F. Fay, T. Reiner, Z. A. Fayad, W. E. Hennink, J. M. Metselaar, W. J. M. Mulder, G. Storm, A systematic comparison of clinically viable nanomedicines targeting HMG-CoA reductase in inflammatory atherosclerosis. *J. Control. Release* **262**, 47–57 (2017).

10. C. Pérez-Medina, J. Tang, D. Abdel-Atti, B. Hogstad, M. Merad, E. A. Fisher, Z. A. Fayad, J. S. Lewis, W. J. M. Mulder, T. Reiner, PET imaging of tumor-associated macrophages with ^{89}Zr-labeled high-density lipoprotein nanoparticles. *J. Nucl. Med.* **56**, 1272–1277 (2015).

11. www.fda.gov/downloads/Drugs/Guidances/UCM078932.pdf.

12. C. Pérez-Medina, T. Binderup, M. E. Lobatto, J. Tang, C. Calcagno, L. Giesen, C. H. Wessel, J. Witjes, S. Ishino, S. Baxter, Y. Zhao, S. Ramachandran, M. Eldib, B. L. Sánchez-Gaytán, P. M. Robson, J. Bini, J. F. Granada, K. M. Fish, E. S. G. Stroes, R. Duivenvoorden, S. Tsimikas, J. S. Lewis, T. Reiner, V. Fuster, A. Kjær, E. A. Fisher, Z. A. Fayad, W. J. M. Mulder, In vivo PET imaging of HDL in multiple atherosclerosis models. *JACC Cardiovasc. Imaging* **9**, 950–961 (2016).

13. C. L. Ventola, Progress in nanomedicine: Approved and investigational nanodrugs. *P T* **42**, 742–755 (2017).

14. Z. A. Fayad, V. Mani, M. Woodward, D. Kallend, M. Abt, T. Burgess, V. Fuster, C. M. Ballantyne, E. A. Stein, J.-C. Tardif, J. H. F. Rudd, M. E. Farkouh, A. Tawakol; dal-PLAQUE Investigators, Safety and efficacy of dalcetrapib on atherosclerotic disease using novel non-invasive multimodality imaging (dal-PLAQUE): A randomised clinical trial. *Lancet* **378**, 1547–1559 (2011).

Binderup *et al.*, *Sci. Transl. Med.* **11**, eaaw7736 (2019)   21 August 2019

12 of 13

15. C. R. Sirtori, The pharmacology of statins. *Pharmacol. Res.* **88**, 3–11 (2014).

16. P. M. Ridker, B. M. Everett, T. Thuren, J. G. MacFadyen, W. H. Chang, C. Ballantyne, F. Fonseca, J. Nicolau, W. Koenig, S. D. Anker, J. J. P. Kastelein, J. H. Cornel, P. Pais, D. Pella, J. Genest, R. Cifkova, A. Lorenzatti, T. Forster, Z. Kobalava, L. Vida-Simiti, M. Flather, H. Shimokawa, H. Ogawa, M. Dellborg, P. R. F. Rossi, R. P. T. Troquay, P. Libby, R. J. Glynn, Antiinflammatory therapy with canakinumab for atherosclerotic disease. *N. Engl. J. Med.* **377**, 1119–1131 (2017).

17. E. J. Folco, Y. Sheikine, V. Z. Rocha, T. Christen, E. Shvartz, G. K. Sukhova, M. F. Di Carli, P. Libby, Hypoxia but not inflammation augments glucose uptake in human macrophages: Implications for Imaging atherosclerosis with [18]fluorine-labeled 2-deoxy-D-glucose positron emission tomography. *J. Am. Coll. Cardiol.* **58**, 603–614 (2011).

18. M. Zamanian-Daryoush, D. Lindner, T. C. Tallant, Z. Wang, J. Buffa, E. Klipfell, Y. Parker, D. Hatala, P. Parsons-Wingerter, P. Rayman, M. S. S. Yusufishaq, E. A. Fisher, J. D. Smith, J. Finke, J. A. DiDonato, S. L. Hazen, The cardioprotective protein apolipoprotein A1 promotes potent anti-tumorigenic effects. *J. Biol. Chem.* **288**, 21237–21252 (2013).

19. J. P. Holland, Y. Sheh, J. S. Lewis, Standardized methods for the production of high specific-activity zirconium-89. *Nucl. Med. Biol.* **36**, 729–739 (2009).

20. H. C. Kolb, H. C. Padgett, S. Zigler, J. Patanella, F. Mu, U. B. Gangadharmath, V. P. Mocharla, P. J. H. Scott, J. C. Walsh, in *Radiochemical Syntheses* (John Wiley & Sons Inc., 2012), pp. 21–30.

21. P. Scott, X. Shao, R. Hoareau, B. Hockley, Modification of fluorine-18 synthesis modules to enable cGMP synthesis of radiopharmaceuticals using multiple radiochemical strategies. *J. Nucl. Med.* **51** (suppl. 2), 1453 (2010).

22. A. S. Plump, J. D. Smith, T. Hayek, K. Aalto-Setälä, A. Walsh, J. G. Verstuyft, E. M. Rubin, J. L. Breslow, Severe hypercholesterolemia and atherosclerosis in apolipoprotein E-deficient mice created by homologous recombination in ES cells. *Cell* **71**, 343–353 (1992).

23. Y. Nakashima, A. S. Plump, E. W. Raines, J. L. Breslow, R. Ross, ApoE-deficient mice develop lesions of all phases of atherosclerosis throughout the arterial tree. *Arterioscler. Thromb.* **14**, 133–140 (1994).

24. M. E. Lobatto, C. Calcagno, J. M. Metselaar, G. Storm, E. S. G. Stroes, Z. A. Fayad, W. J. M. Mulder, Imaging the efficacy of anti-inflammatory liposomes in a rabbit model of atherosclerosis by non-invasive imaging. *Methods Enzymol.* **508**, 211–228 (2012).

25. M. L. Senders, M. E. Lobatto, R. Soler, O. Lairez, C. Pérez-Medina, C. Calcagno, Z. A. Fayad, W. J. M. Mulder, F. Fay, in *Methods in Molecular Biology* (Springer, 2018), vol. 1816, pp. 385–400.

26. J. F. Granada, K. Milewski, H. Zhao, J. J. Stankus, A. Tellez, M. S. Aboodi, G. L. Kaluza, C. G. Krueger, R. Virmani, L. B. Schwartz, A. Nikanorov, Vascular response to zotarolimus-coated balloons in injured superficial femoral arteries of the familial hypercholesterolemic swine. *Circ. Cardiovasc. Interv.* **4**, 447–455 (2011).

27. Y. Kim, F. Fay, D. P. Cormode, B. L. Sanchez-Gaytan, J. Tang, E. J. Hennessy, M. Ma, K. Moore, O. C. Farokhzad, E. A. Fisher, W. J. M. Mulder, R. Langer, Z. A. Fayad, Single step reconstitution of multifunctional high-density lipoprotein-derived nanomaterials using microfluidics. *ACS Nano* **7**, 9975–9983 (2013).

28. C. Pérez-Medina, D. Abdel-Atti, Y. Zhang, V. A. Longo, C. P. Irwin, T. Binderup, J. Ruiz-Cabello, Z. A. Fayad, J. S. Lewis, W. J. M. Mulder, T. Reiner, A modular labeling strategy for in vivo PET and near-infrared fluorescence imaging of nanoparticle tumor targeting. *J. Nucl. Med.* **55**, 1706–1711 (2014).

Binderup *et al.*, *Sci. Transl. Med.* **11**, eaaw7736 (2019)   21 August 2019

13 of 13

Science Translational Medicine

Imaging-assisted nanoimmunotherapy for atherosclerosis in multiple species

Tina Binderup, Raphaël Duivenvoorden, Francois Fay, Mandy M. T. van Leent, Joost Malkus, Samantha Baxter, Seigo Ishino, Yiming Zhao, Brenda Sanchez-Gaytan, Abraham J. P. Teunissen, Yohana C. A. Frederico, Jun Tang, Giuseppe Carlucci, Serge Lyashchenko, Claudia Calcagno, Nicolas Karakatsanis, Georgios Soultanidis, Max L. Senders, Philip M. Robson, Venkatesh Mani, Sarayu Ramachandran, Mark E. Lobatto, Barbara A. Hutten, Juan F. Granada, Thomas Reiner, Filip K. Swirski, Matthias Nahrendorf, Andreas Kjaer, Edward A. Fisher, Zahi A. Fayad, Carlos Pérez-Medina and Willem J. M. Mulder

Particle production

Scale-up is a nontrivial part of translating a therapy from preclinical work in small animal models toward clinical utility. Binderup, Duivenvoorden, Fay, and colleagues previously developed simvastatin-loaded high-density lipoprotein (S-HDL) particles that inhibited macrophage proliferation in the blood vessel walls of mouse models of atherosclerosis. Here, they tested methods to produce large amounts of S-HDL needed for larger animal studies and imaging protocols to evaluate therapeutic efficacy. The scaled-up particles showed anti-inflammatory effects in the blood vessels of rabbit and porcine models of atherosclerosis, reducing vessel wall enlargement. This study highlights challenges encountered when scaling a nanoimmunotherapy for use in larger animal models and strategies to overcome these challenges.

ARTICLE TOOLS	http://stm.sciencemag.org/content/11/506/eaaw7736
SUPPLEMENTARY MATERIALS	http://stm.sciencemag.org/content/suppl/2019/08/19/11.506.eaaw7736.DC1
RELATED CONTENT	http://stm.sciencemag.org/content/scitransmed/7/275/275ra20.full http://stm.sciencemag.org/content/scitransmed/6/239/239sr1.full http://stm.sciencemag.org/content/scitransmed/8/333/333ra50.full http://stm.sciencemag.org/content/scitransmed/12/531/eaaw1868.full http://stm.sciencemag.org/content/scitransmed/12/546/eaaz2294.full
REFERENCES	This article cites 25 articles, 8 of which you can access for free http://stm.sciencemag.org/content/11/506/eaaw7736#BIBL
PERMISSIONS	http://www.sciencemag.org/help/reprints-and-permissions

Use of this article is subject to the Terms of Service